

UC Berkeley

UC Berkeley Previously Published Works

Title

Extreme In-Plane Thermal Conductivity Anisotropy in Titanium Trisulfide Caused by Heat-Carrying Optical Phonons

Permalink

<https://escholarship.org/uc/item/49d7621d>

Journal

Nano Letters, 20(7)

ISSN

1530-6984

Authors

Liu, Huili
Yu, Xiaoxia
Wu, Kedi
[et al.](#)

Publication Date

2020-07-08

DOI

10.1021/acs.nanolett.0c01476

Peer reviewed

Extreme in-plane thermal conductivity anisotropy in titanium trisulfide caused by heat-carrying optical phonons

Huili Liu^{†,‡,§}, Xiaoxia Yu^{‡,§}, Kedi Wu[¶], Yang Gao^{†,‡}, Sefaattin Tongay[¶], Ali Javey^{†,‡}, Lidong Chen^{‡,*}, Jiawang Hong^{‡,*} and Junqiao Wu^{†,‡,*}

[†]Materials Sciences Division, Lawrence Berkeley National Laboratory, Berkeley, California 94720, USA

[‡]Department of Materials Science and Engineering, University of California, Berkeley, California 94720, USA

[§]School of Aerospace Engineering, Beijing Institute of Technology, Beijing 100081, China

[¶]School for Engineering of Matter, Transport, and Energy, Arizona State University, Tempe, Arizona 85287, USA

[‡]Department of Electrical Engineering and Computer Science, University of California, Berkeley, California 94720, USA

[€]Shanghai Institute of Ceramics, Chinese Academy of Sciences, Shanghai, 200050, China

ABSTRACT: Layered materials are defined by covalent in-plane bonding and van der Waals cross-plane interactions, resulting in high in-plane versus cross-plane anisotropy in physical properties. In contrast, anisotropy between the two in-plane directions is typically weak or absent, as atoms are bonded covalently along both in-plane directions. However, in materials with large structural difference along these two in-plane directions, high in-plane anisotropies in physical properties can also arise. We report such a case in layered TiS_3 , which features tightly bonded atomic chains along the b-axis direction, held together by weaker, inter-chain bonding along the a-axis direction. Experiments show thermal conductivity along the chain twice as high as between the chain, an in-plane anisotropy higher than any other layered materials measured to date. Interestingly, its acoustic phonons do not exhibit considerable anisotropy between these two directions. We found that in contrast to most other materials, optical phonons in TiS_3 conduct an unusually high portion of heat (up to 66% along the b-axis direction), carried by highly dispersive optical phonon modes. The large dispersiveness of optical phonons along the chains, contrasted

to much less dispersive optical phonons perpendicular to the chains, is the primary reason for the observed high anisotropy in thermal conductivity. The finding discovers materials with unusual thermal conduction mechanism, as well as provides new material platforms for potential heat-routing or heat-managing devices.

KEYWORDS: *Titanium trisulfide, in-plane anisotropy, optical phonons, thermal conductivity*

Layered materials are held together between layers via weak, van der Waals (vdW) interactions, whereas within each layer the atoms are bonded together by much stronger covalent bonding. They draw tremendous research attention by their fascinating physical properties as a new class of two-dimensional (2D) materials when thinned down to the monolayer. Potential applications of these materials are being investigated for fields ranging from electronics,¹⁻³ catalysis,⁴ and photonics,^{5,6} to sensing^{7,8} and thermoelectrics.⁹ Not surprisingly, the weak inter-layer vdW interactions combined with the strong intra-layer covalent bonding may lead to high anisotropies in properties between the cross-plane and in-plane directions. For example, thermal conductivity (κ) of pyrolytic graphite is 5.7 and 1950 W m⁻¹ K⁻¹ at 300 K for the cross-plane and in-plane directions, respectively.¹⁰ Additionally, it has also been realized that there exist structural anisotropy within the basal plane of most layered materials, such as the difference in armchair (AC) and zigzag (ZZ) structures in black phosphorus (b-P),^{11,12} black arsenic (b-As),¹³ tin selenide (SnSe),¹⁴ and graphene.¹⁵ This would result in modest in-plane anisotropies in thermal, electronic and optical properties, offering potential applications that are not possible with isotropic materials.¹⁶

Recently, layered transition metal trichalcogenides (TMTCs), MX₃ (M=Zr, Ti, and X=S, Se), have become a focus of interest,^{17,18} attributed mostly to their unique, quasi-one dimensional (1D) chain structure in the basal plane.^{19,20} Among them, titanium trisulfide (TiS₃) has a direct bandgap of ~1.0 eV,^{21,22} potentially high electron mobility of over 10,000 cm² V⁻¹ s⁻¹ from *ab initio* calculations,²³ and a high on/off ratio of ~7,000 when made into field effect transistors.²⁴ Experimentally, TiS₃ nanosheets were measured to show distinct carrier mobility of 80 cm² V⁻¹ s⁻¹ and 40 cm² V⁻¹ s⁻¹ along its b- and a-axis directions, respectively.²⁵ Wu *et al* reported a unusual sulfur-sulfur lone-pair vibrational mode of TiS₃.²⁶ Zhang *et al* calculated and found high anisotropy in carrier transport in TiS₃ monolayers for potential thermoelectric application.²⁷ However, an important physical property, thermal conductivity (κ), has not been experimentally characterized in TiS₃, especially any potentially new thermal transport property related to its unique quasi-1D chain structure in the basal plane. In this work, we report an in-plane

anisotropy in κ of TiS_3 up to a ratio of 2, higher than any currently known layered materials, by combining advanced thermal transport measurements with first-principles calculations.

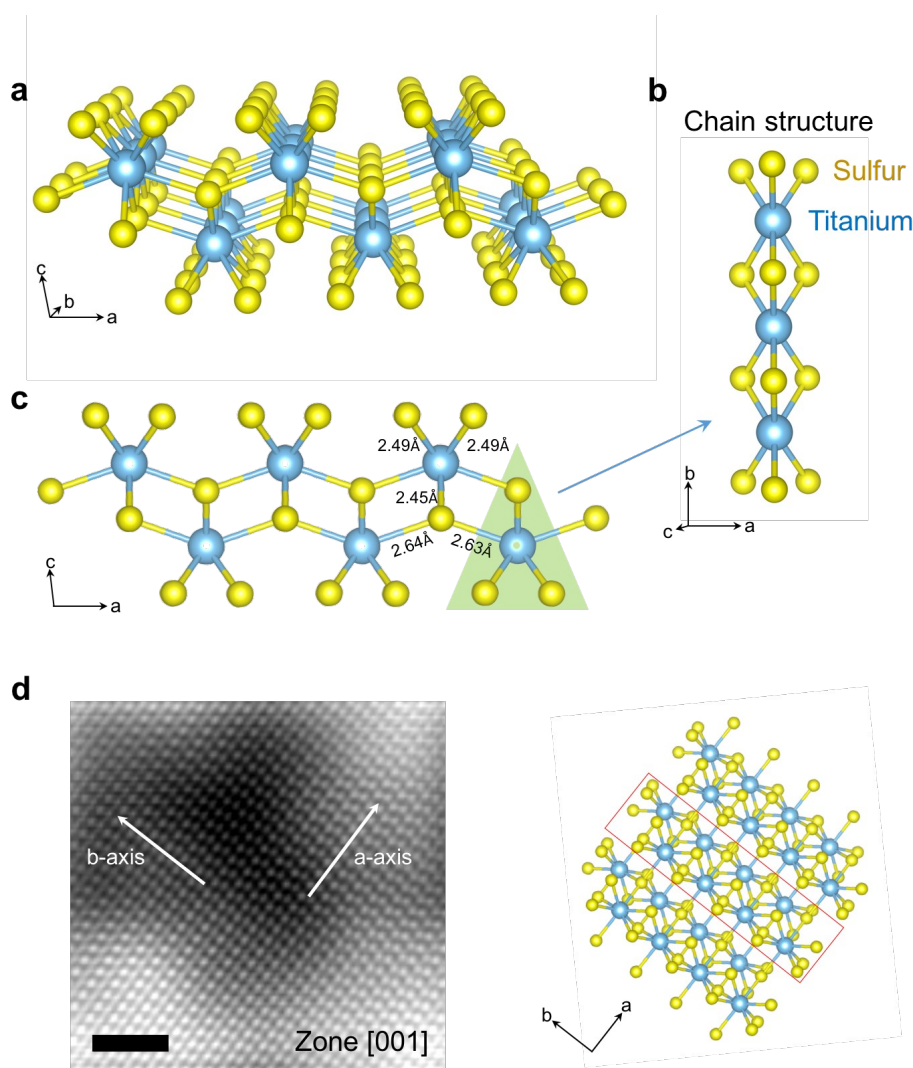


Figure 1. Crystal structure of TiS_3 . (a) Monolayer of TiS_3 . (b) Chain structure along the b-axis. (c) Side view of the monolayer. (d) TEM micrograph imaged along the c-axis (left) and the corresponding schematic structure (right). Red box indicates the chain along the b-axis. Scale bar, 1 nm.

TiS_3 takes a monoclinic structure with the space group of $P2_1/m$ ($a = 4.96\text{\AA}$, $b = 3.40\text{\AA}$, $c = 8.79\text{\AA}$, $\alpha = \gamma = 90^\circ$, $\beta = 97.3^\circ$).²⁸ Figure 1a shows a schematic of the crystal structure of a single layer. Importantly, the basal plane features one-dimensional atomic chains along the b-axis direction, as shown in Figure 1b. The bonding lengths in the chain are 2.45\AA and 2.49\AA ,²⁹ slightly smaller than the sum of the individual covalent radii (1.05\AA and 1.60\AA for S and Ti,³⁰ respectively). The neighboring chains are laterally connected by longer Ti-S bonds along the a-axis as shown in Figure 1c. These

inter-chain bonding lengths are 2.63 Å and 2.64 Å, respectively, nearly equal to the sum of the individual covalent radii. This unique chain structure leads to high electronic, structural and vibrational anisotropies in the basal plane of TiS₃. For the electronic structure, the 3p_x orbitals of S atoms contribute mostly to the top of the valence band, which dominates the band dispersion along the a-axis direction; the 3d_{x²-y²} orbitals of Ti atoms compose the conduction band, dispersing mostly along the b-axis direction.³¹ As shown in Figure S1 (see Supporting Information), TiS₃ single crystals grow naturally into micro-ribbons or whiskers parallel to the b-axis direction.²⁶ Figure 1d is a high-resolution TEM (Transmission Electron Microscopy) image of TiS₃, showing atomic arrangement along the a- and b-axis, consistent with the chain structures seen in the right panel.

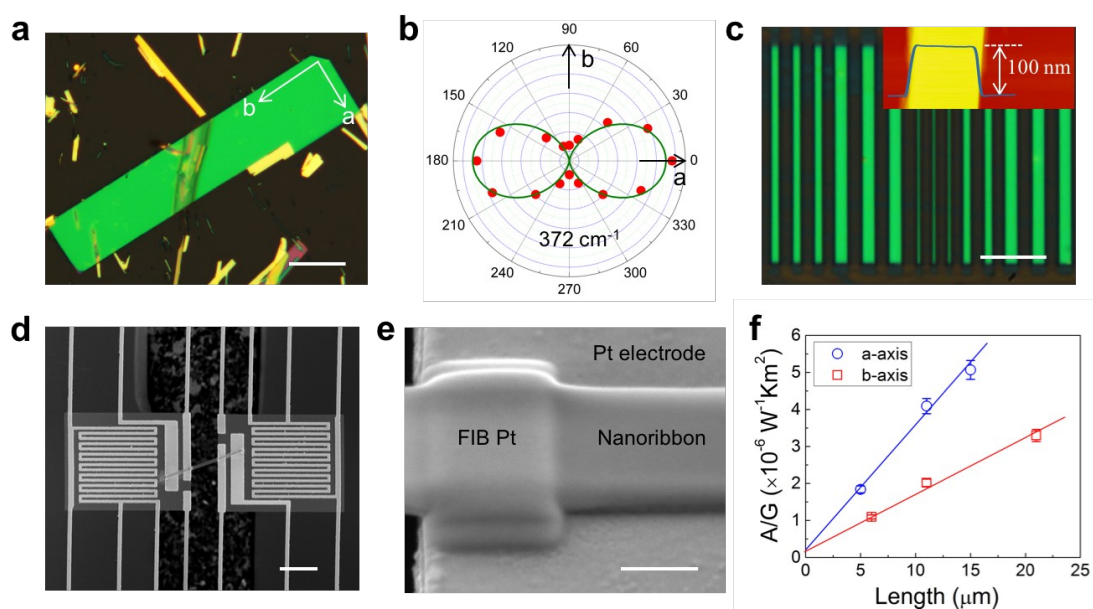


Figure 2. TiS₃ device fabrication for thermal and electrical measurements. (a) Optical image of exfoliated TiS₃ flakes. (b) Angular dependence of the intensity of the A_g Raman mode at 372 cm⁻¹. Solid curve is fitting to determine the crystal orientation along the a-axis and b-axis. (c) Optical image of lithographically patterned TiS₃ nanoribbons. Inset is an AFM (Atomic Force Microscopy) image that shows the thickness of 100 nm. (d) SEM (Scanning Electron Microscopy) image of a suspended micro-pad device supporting a single nanoribbon. (e) SEM image of part of the nanoribbon Pt-bonded onto the underlying electrode by FIB (Focused Ion Beam). (f) Cross-sectional area / thermal conductance (A/G) as a function of the nanoribbon length. Error bars include those from data of thermal conductance and sample size. These nanoribbons were made from the same flake (100 nm thick). The linear relation extrapolating to nearly zero indicates negligible thermal contact resistance for the

measured nanoribbons devices. Scale bars, 50 μm (a); 10 μm (c), (d); 500 nm (e).

Figure 2a shows a TiS_3 flake mechanically exfoliated from the bulk crystal, where the crystallographic orientations were confirmed by micro-Raman analysis, as the Raman signal intensity depends on the angle between the laser polarization direction and the TiS_3 crystal orientation.¹⁸ Raman intensity of the most prominent peak¹⁸ ($\sim 372\text{ cm}^{-1}$) was fitted by theoretical angular dependence, $I \propto \cos^2\phi$, shown as a solid curve in Figure 2b, where $\phi = 0^\circ$ (90°) corresponds to the a- (b-) axis direction of TiS_3 . Details of device fabrication and measurements were published previously.^{11, 12} Figure 2c shows a set of a-axis-oriented TiS_3 nanoribbons of length $\sim 40\ \mu\text{m}$ and width varying from ~ 0.5 to $\sim 2\ \mu\text{m}$, e-beam lithographically patterned from a single flake with a thickness of 100 nm. These individual nanoribbons were carefully dry-transferred onto the two suspended micro-pads to bridge them. To further improve the electrical and thermal contact, a small amount of Pt metal was deposited by focused ion beam (FIB) to bond the end of the nanoribbon to the underneath metal electrodes (Figure 2d and 2e). Indeed, the electrical contact resistance is reduced after the FIB Pt deposition, as shown in Figure S2 (see Supporting Information). All measurements were performed under high vacuum ($<10^{-6}$ torr) with radiation shield.³²⁻³⁴ Figure 2f shows cross-sectional area divided by thermal conductance (A/G) as a function of the nanoribbon length (L), where a linear relationship is seen and extrapolated to nearly zero A/G at $L = 0$, proving negligible contact thermal resistance for these nanoribbons devices. The flexible and suspended nature of the device also maximally releases any tensile, shearing and torsional stress potentially built up in the nanoribbon, as well as eliminates substrate influence, during the measurements.

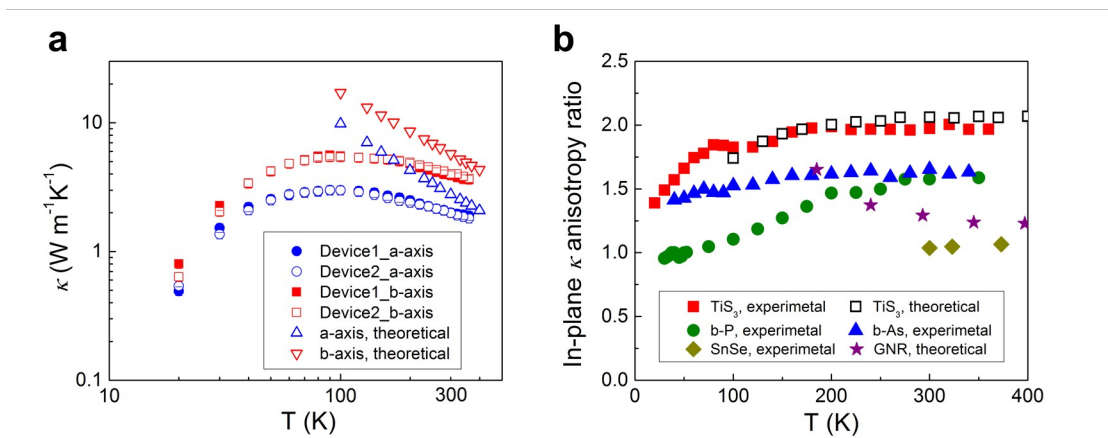


Figure 3. In-plane thermal conductivity (κ) of TiS_3 and its anisotropy. (a) Both measured and calculated temperature

dependence of κ along the a- and b-axis. (b) In-plane anisotropy ratio of κ , defined as κ_b/κ_a for TiS_3 (this work), compared to the same of κ_{ZZ}/κ_{AC} for b-P (170 nm thick nanoribbon, experimental), b-As (124 nm thick nanoribbon, experimental), SnSe (bulk, experimental), and graphene nanoribbon (GNR, theoretical).

Figure 3a shows the temperature dependence of κ measured along the a- (defined as κ_a) and b-axis (κ_b) directions. It is found that κ_b is much higher than κ_a near room temperature, but they gradually become similar at lower temperatures. As shown in Figure 3b, the anisotropic ratio of κ ($=\kappa_b/\kappa_a$) remains nearly a constant of ~ 2.0 between $T \sim 150$ K and 360 K, but at $T < \sim 150$ K the ratio is reduced toward ~ 1.4 at $T \sim 20$ K. As a comparison, we show the in-plane anisotropy in κ of b-P,¹¹ b-As,¹³ SnSe,¹⁴ and graphene nanoribbon (GNR),³⁵ as they also possess structural anisotropy along their zigzag (ZZ) and armchair (AC) directions in the basal plane. Their κ anisotropy (κ_{ZZ}/κ_{AC}) at 300 K is ~ 1.6 for b-P and b-As, ~ 1.0 for SnSe, and ~ 1.3 for GNR. It is clear that TiS_3 hosts the highest in-plane anisotropy in κ compared to all other layered materials. Because the electrical conductivity of these TiS_3 nanoribbons are very low, about $\sim 80 \text{ S m}^{-1}$ and $\sim 90 \text{ S m}^{-1}$ along the a- and b-axis at 300 K, respectively (Figure S3 in Supporting Information), electronic contributions to κ is negligible, and the measured κ is therefore dominated by lattice thermal conductivity. Unlike the structural anisotropy arising from the ZZ versus AC bonding in b-P, b-As, SnSe, and GNR, the quasi-1D chain structure of TiS_3 is suspected to be responsible for this unusually high κ anisotropy in its basal plane.

To elucidate the physical mechanism of the anisotropic thermal conductivity in TiS_3 , we calculated the phonon dispersion and thermal transport properties using density function theory (DFT) and phonon Boltzmann transport equations. Figure 4a shows the phonon dispersion of TiS_3 along the Γ -Y (a-axis) and Γ -Z (b-axis) directions in the first Brillouin zone. These results are consistent with first-principles calculations of monolayer TiS_3 reported by Zhang et al.²⁷

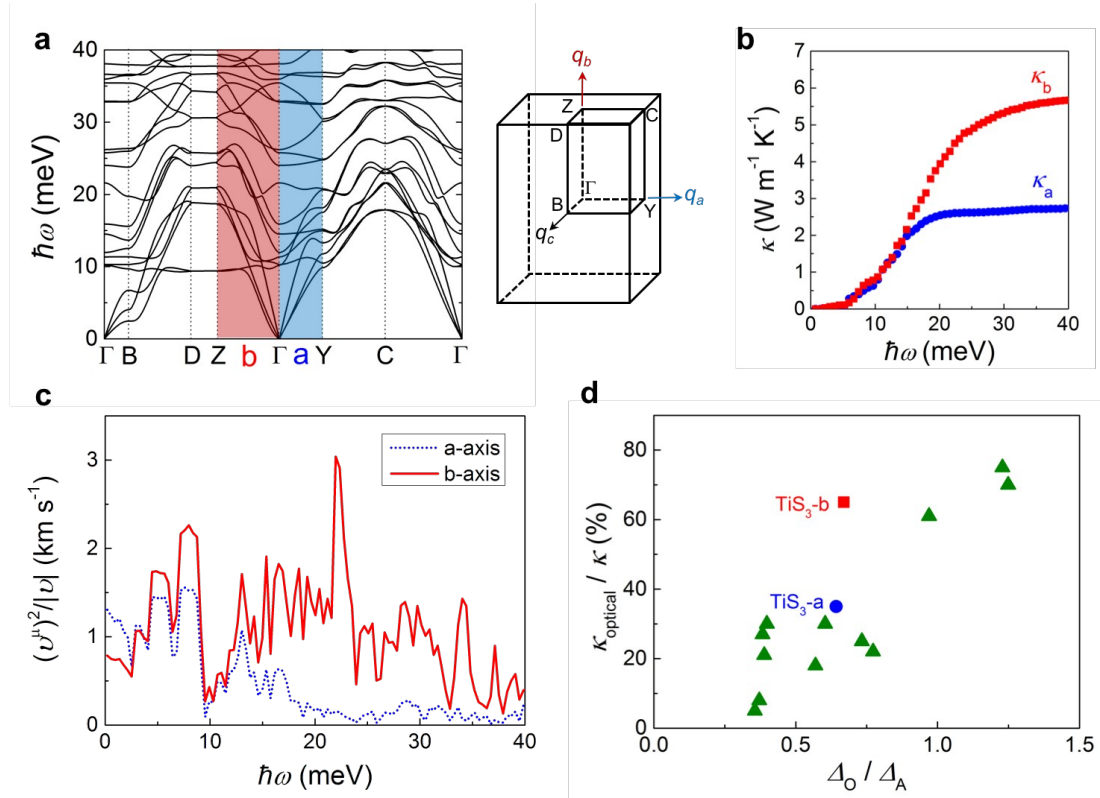


Figure 4. DFT calculation of phonon properties of TiS_3 . (a) Phonon dispersion of TiS_3 . The right panel shows the Brillouin zone of TiS_3 . (b) Energy dependence of cumulative lattice thermal conductivity along the a- and b-axis at 300 K. (c) Average group velocity of phonon modes along the a- and b-axis, respectively, showing high anisotropy for optical phonons between 15 and 30 meV. (d) Calculated percentage of optical phonon contribution to total thermal conductivity, plotted as a function of bandwidth of the most dispersive optical phonon normalized by the bandwidth of acoustic phonons. The materials are listed in Table 1.

The lattice thermal conductivity tensor, relating temperature gradient in the ν direction to heat current per unit area in the μ direction through Fourier's law, is a summation of contributions from all phonon modes (j) over wavevectors (\mathbf{q}) in the first Brillouin zone,³⁶ written as

$$\kappa_{\mu\nu} = \frac{1}{3} \sum_{\lambda} c_{\lambda} v_{\lambda,\mu} v_{\lambda,\nu} \tau_{\lambda}, \quad (1)$$

Where the index $\lambda = j, \mathbf{q}$, c_{λ} is specific heat capacity, $v_{\lambda,\mu}$ is phonon group velocity in the μ direction, and τ_{λ} is phonon relaxation time. The first suspect that may cause the large anisotropy in κ would be anisotropy in acoustic phonon group velocity or anharmonicity, as demonstrated in the case of b-P.¹¹ However, from the dispersion relation in Figure 4a, it can be seen that the acoustic phonon group

velocity does not differ significantly along the a- and b-axis directions. Indeed, as shown in Table S1 (see Supporting Information), the averaged group velocity of acoustic phonons is calculated to $v_A = 4.44 \text{ km s}^{-1}$ and 4.79 km s^{-1} along the a- and b-axis, respectively. These values differ by only $\sim 8\%$, or if comparing the velocity squared (v_A^2), differ by only $\sim 16\%$. This is far lower than the observed anisotropy in κ by a factor of two. The anharmonicity of phonons is characterized by the Gruneisen parameter and enables the typical three-phonon processes, which defines τ_λ at temperatures higher than the Debye temperature. However, these phonon-phonon scattering processes sample phonon modes in all phase space that is allowed by energy conservation and the Umklapp momentum restriction, effectively mixing the lattice anharmonicity along all crystal directions. Therefore, we conclude that acoustic phonons are not the primary reason for the observed two-fold in-plane anisotropy in κ .

We now focus on contributions from the optical phonons. First, we calculated the cumulative lattice thermal conductivity along a- and b-axis at 300 K as a function of phonon energy, taking into account all three-phonon scattering processes. The results are shown in Figure 4b, where κ_b is cumulated to $5.78 \text{ W m}^{-1} \text{ K}^{-1}$, and κ_a to $2.84 \text{ W m}^{-1} \text{ K}^{-1}$ (Table S2, see Supporting Information), giving rise to the theoretical anisotropy ratio of ~ 2 in Figure 3b. At this temperature or higher ($k_B T > \sim 26 \text{ meV}$), the optical phonons along both directions, having energies of $10 \sim 30 \text{ meV}$, are nearly fully thermally activated. More importantly, it is clear that for all phonon energies $< \sim 15 \text{ meV}$, *i.e.*, mostly acoustic phonons, κ_a and κ_b show nearly identical cumulative values. They start to deviate from each other only when the phonon energy is higher than $\sim 15 \text{ meV}$, sampling into the optical phonon branches (Figure 4a). It can be also concluded from Figure 4b that optical phonons carried heat contributes to κ by $\kappa_{\text{optical}}/\kappa \sim 34\%$ and $\sim 66\%$ along the a- and b-axis, respectively.

The questions arising are then (1) why optical phonons contribute to κ by such a unusually high fraction in TiS_3 , and (2) why such contribution differs so much for heat flowing along a- and b-axis.

Crystals with complex unit cell structures have a large number of optical phonon modes, and they account for a high fraction of the phonon density of states. However, they typically contribute negligibly to thermal conductivity due to their low group velocities and short lifetimes.³⁷ In rare cases when optical phonons become dispersive with considerable group velocities, they may contribute significantly to the total thermal conductivity. For example, it has been recently shown that optical phonons account for 22% of κ in PbTe ,³⁸ 25% in PbSe ,³⁸ 30% in Mg_2Si ,³⁹ and 75% in hexagonal

Ge₂Sb₂Te₅.⁴⁰ We found that TiS₃ is another example for such case. Figure 4a shows that between 10 and 30 meV, there exist a large number of dispersive optical phonon modes along both the a- and b-axis direction. Especially along the b-axis direction (Γ-Z), the optical phonon modes exhibit dispersions with a slope that is nearly parallel to those of the acoustic modes, indicating an unusually high optical phonon group velocity (v_o) that is comparable to that of the acoustic phonons (v_A). The values of these velocities are compared in Table S1 (see Supporting Information).

Following Mukhopadhyay *et al*,⁴⁰ we calculated and show in Figure 4c the energy-dependent group velocity averaged over all phonon modes along the a- and b-axis directions. This averaged velocity is calculated by

$$\dot{v}(\omega) = \frac{(v^\mu)^2}{|v|}(\omega) = \left(\frac{\Delta q}{2\pi}\right)^3 \sum_\lambda \frac{(v_\lambda^\mu)^2}{|v_\lambda^\mu|} \delta(\omega - \omega_\lambda) / \sum_j g_j(\omega), \quad (2)$$

where v_j^μ is the phonon group velocity of phonon mode j at wavevector \mathbf{q} along the μ -axis, and $g_j(\omega)$ denotes phonon density of states. Two major features are evident from Figure 4c: (I) optical phonons (between 10 ~ 30 meV) exhibit considerable group velocity, comparable to that of acoustic phonons (between 0 ~ 15 meV), and (II) this effect is much more pronounced along b- than a-axis direction, showing a high anisotropy attributed mostly to optical phonons, rather than acoustic phonons.

The effect (I) is related to the high dispersiveness of the optical phonons. In a simple 1D di-atomic chain model,⁴¹ a highly dispersive optical phonon mode requires strong intra-cell bonding and that the two atoms do not have extreme mass ratio. Contrasted to these, the acoustic phonon group velocity depends on inter-cell bonding and total mass in the unit cell. These conditions are all reasonably satisfied in TiS₃. To have a high $\kappa_{\text{optical}}/\kappa$, it is also preferred that the contribution of acoustic phonons to κ (κ_{acoustic}) is low. This is indeed the case in TiS₃, where the acoustic phonons are expected to be scattered strongly via the three-phonon processes. The absence of bandgap between acoustic and optical phonons in Figure 4a facilitates the scattering of acoustic phonons by optical phonons (the so-called aao process, where 'a' and 'o' represent acoustic and optical phonons, respectively);⁴² the well-separated (*i.e.*, non-bunched) acoustic phonon lines provide large phase space for the scattering of acoustic phonons by each other (the so-called aaa process).⁴² Taken together, these effects cause an unusually high $\kappa_{\text{optical}}/\kappa$ in TiS₃.

The effect (II) is attributed to the different bonding length and bonding configuration along the a- and b-axis crystallographic directions. As seen in Figure 4a, the optical phonon dispersions

along the a-axis are in general flatter than along the b-axis, although several dispersive modes are also seen. This can be partially explained by the larger lattice constant, hence narrower Brillouin zone along the a-axis. Symmetry rules impose the requirement of zero slopes for these phonon modes at the zone center and boundary (e.g., at Γ , Y and Z in Figure 4a), therefore, a narrower zone would naturally lead to flatter optical bands and consequently lower optical phonon group velocities. This effect shares the same origin as in GaAs/AlAs superlattices,⁴³ where in the cross-plane direction GaAs and AlAs were grown in periods equal to n times the natural unit cell of their bulk counterparts. The Brillouin zone is then folded along the cross-plane direction to a width that is $1/n$ times of the in-plane zone width, resulting in strong suppression of optical phonon group velocity in the cross-plane direction. A similar effect exists now along the a- and b-axis directions in TiS_3 , although both are in-plane. Aside from the high anisotropy in group velocity, optical phonons along these two directions do not differ much in their contribution to all three-phonon scattering processes. We calculated the relaxation lifetime of all three-phonon scattering (aaa, aao, aoo, and ooo) processes, and the contributions to these processes from a- and b-axis optical phonons, and show the results in Figure S5 (see Supporting Information). It can be seen that the optical phonons along these two directions do not differ significantly in their contribution to these processes. This finding further confirms the conclusion that it is the anisotropy in group velocity of the optical phonons, rather than their role in scattering acoustic phonons, that causes the large κ_b/κ_a in TiS_3 .

At the atomic scale, the strong in-plane anisotropy of thermal conductivity results from the distinct atomic bonding configurations. As shown in Figure 1, only two Ti-S bonds exist along the a-axis direction between any two Ti atoms, while there are six Ti-S bonds along the b-axis direction. Moreover, the strong anisotropy of optical phonons is reflected by the strong anisotropy of the electronic polarizability of TiS_3 . We calculated the Born effective charge $(e^*)_{l,\mu\nu}$ of TiS_3 , which reflects the force of the atom l along μ -direction, under the electric field along ν -direction.⁴⁴ The diagonal components of the in-plane Born effective charge tensors are shown in Table S3 (see Supporting Information), which shows that $(e^*)_{bb}$ is much larger than $(e^*)_{aa}$ for all Ti and S atoms. For example, for the Ti1(Ti2) and S3(S4) atoms, the ratio of $(e^*)_{bb}/(e^*)_{aa}$ is $2 \sim 3$, while for the atoms S1(S2) and S5(S6), $(e^*)_{aa}$ are even smaller compared to $(e^*)_{bb}$. As is well known, the optical modes correspond to the opposite displacement of positive and negative charged atoms, generating internal electric fields in the crystal. The magnitude of the restoration force of each atom depends on its Born effective charge. Consequently, the interactions along the b-axis will be stronger than those along the a-axis direction. The optical phonons are usually

closely related to the dielectric permittivity. Therefore, it is expected that the dielectric constant would also be highly anisotropic in TiS_3 . Indeed, our DFT results show that the static dielectric constant in TiS_3 are 12.51 and 33.15 along its a- and b-axis directions, respectively.

We also calculated the temperature dependence of κ along the two in-plane directions using DFT, including all possible phonon-phonon interactions but not phonon-impurity and phonon-boundary scatterings. As shown in Figure 3, although the values of the calculated κ are slightly higher than the measured values, their ratio, κ_b/κ_a , agrees well with the measurements.

		Mass ratio, m/M	Debye temp. (K)	Max acoustic bandwidth, Δ_A (meV)	Max optical bandwidth, Δ_O (meV)	κ (W/m-K), 300K	$\kappa_{\text{optical}}/\kappa$ (%), 300K	Reference
TiS_3	b-axis	0.67	-	20.9	14.0	5.78	66	This work
	a-axis			13.9	8.9	2.84	34	
	Si	1.0	710	51.1	18.2	145	5	Broido et al. ³⁶
	Ge	1.0	415	29.4	10.9	60	8	Broido et al. ³⁶
b-P	zigzag	1.0	278	24.0	9.2	30.1	27	Qin et al. ⁴⁵
	armchair			15.6	6.0	13.6	21	Qin et al. ⁴⁵
	PbSe	0.38	170	12.7	9.3	2.2	25	Tian et al. ³⁸
	PbTe	0.62	140	11.5	4.0	2.0	22	Tian et al. ³⁸
	Bi_2Te_3 , in-plane	0.61	162	7.0	4.2	1.2	30	Hellman et al. ⁴⁶
	$\text{Ge}_2\text{Sb}_2\text{Te}_5$, in-plane	0.58	100	5.8	7.1	1.7	75	Mukhopadhyay et al. ⁴⁰
	Mg_2Si	0.86	432	35.2	14.0	11.3	30	Li et al. ³⁹
	Mg_2Sn	0.20	273	14.6	8.3	7.2	18	Li et al. ³⁹
	SnSe, zigzag	0.66	210	6.9	6.7	2.0	61	Guo et al. ⁴⁷
	SnS, zigzag	0.27	270	8.0	10.0	2.3	70	Guo et al. ⁴⁷

Table 1. Comparison of properties of selected materials. Δ_O and Δ_A are bandwidth of the most dispersive optical and acoustic phonons from calculated dispersion relation.

We now compare all reported materials that show high percentage of $\kappa_{\text{optical}}/\kappa$ in an attempt to find properties in common. As seen from Eq. (1), it is not surprising that these materials typically have at least one optical phonon branch that is highly dispersive and thus has high group velocity to carry heat flow. The high dispersiveness would lead to large bandwidth for that phonon mode over the Brillouin zone. We define the normalized bandwidth (Δ_O/Δ_A) as the bandwidth of the most dispersive optical phonon (Δ_O) divided

by that (Δ_A) of the most dispersive acoustic phonon. In a simple diatomic chain model, a high Δ_O/Δ_A prefers similar masses of the two atoms, as well as stronger spring constant for vibration modes involving the lighter atoms than for the heavier atoms. From published calculated phonon dispersions of a selected set of materials including TiS_3 (Table 1), we plot in Figure 4d $\kappa_{\text{optical}}/\kappa$ as a function of Δ_O/Δ_A . A positive correlation can be seen between these two quantities. The data scattering reflects factors missing in the plot: the lifetime ratio between optical and acoustic phonons differ in different materials, and only the single, most dispersive optical and acoustic phonons are considered. Nevertheless, the approximate correlation shows that optical phonons may contribute a large portion to lattice thermal conductivity in materials with one or more highly dispersive optical phonons.

In conclusion, we found an extreme anisotropy, by a factor of two and higher than that of any existing layered materials, in the in-plane thermal conductivity in TiS_3 . This occurs between the quasi-1D chain direction and the inter-chain direction in the basal plane of this layered material. First-principles calculations reveal that, unlike most materials where heat is mostly transported by acoustic phonons, in TiS_3 the optical phonons carry an unusually high portion of heat, up to 66% along the chain direction, owing to highly dispersive optical phonons. Perpendicular to the chain direction, on the other hand, the optical phonons are less dispersive and contribute to a much lower 34% of thermal conductivity. With such highly anisotropic thermal transport in the basal plane, layered TiS_3 may serve as a platform for designing novel devices to route heat flow at the nanoscale, such as thermal switch, regulator, or diodes.⁴⁸

Experimental Section. *TiS₃ nanoribbon device fabrication.* As reported previously,^{11, 12} TiS_3 flakes were mechanically exfoliated onto a SiO_2/Si substrate using PDMS (Polydimethylsiloxane), and then tailored into nanoribbons (0.5 ~ 2 μm in width and 25 ~ 40 μm in length) using electron-beam lithography (EBL) followed by reactive ion etching (RIE). Specifically, the flakes were coated by PMMA (Poly(methyl methacrylate), C4-950, 4000 rpm) and baked at 180 °C for 5 mins. The PMMA was patterned with EBL followed by a developing process using MIBK : IPA = 1 : 3 for 1 min. The exposed TiS_3 was etched via RIE using a mixed gas (90% SF_6 and 10% O_2 , 60 sccm) for several seconds. After the PMMA removal with acetone and rinsing by isopropyl alcohol, TiS_3 nanoribbons were obtained. Selected individual nanoribbon was manually dry-transferred onto an empty, suspended-pad micro-device using a sharp Tungsten needle (600 nm tip diameter, Cascade Microtech). A small amount of platinum was directly deposited to bond the nanoribbon onto the underlying Pt electrodes using a FIB (dual-beam FEI Quanta). The thickness of the nanoribbon was confirmed by Atomic Force

Microscope (AFM). After the Pt deposition, the electrical quality of the electrodes was verified by a linear I-V relationship (ohmic contact). The devices were annealed at 373 K for one hour in vacuum to further improve electrical and thermal contacts at the electrodes.

Thermal and electrical measurements. The thermal resistance, electrical conductance, and Seebeck coefficient of nanoribbons were measured using the suspended-pad micro-devices technique following previous reports.^{32, 34} Two SiN_x pads with Pt electrodes were suspended by long and flexible SiN_x arms (~400 μm). Pt serpentine electrodes on the pads were for micro-heater and thermometers, and additional four Pt electrodes were for electrical resistance and thermopower measurements. A DC current ($I = 0\sim 15\ \mu\text{A}$) was applied to the micro-heater for the temperature raising (hot pad) of ΔT_h , and the other pad (cold pad) sensed a temperature of ΔT_s through the nanoribbon. An external heater (Lakeshore 335 Temperature Controller) and cryogenic compressor cooler (HC-4A, Sumitomo CRYOGENICS) controlled the global temperature in the chamber, which was under high vacuum ($< 10^{-6}$ Torr) during the measurements. An AC current with a small amplitude of ~ 500 nA and frequency of 1.1 kHz (199 Hz) was applied to probe ΔT_h (ΔT_s) on the hot (cold) pad using Lock-in amplifiers. The thermal conductance of the nanoribbon (G) is given by $G = (P \times \Delta T_s) / (\Delta T_h^2 - \Delta T_s^2)$, where P is the heating power, $P = I^2 \times (R_h + R_{arm})$, and R_h and R_{arm} are the resistance of heating Pt electrodes and arms, respectively. Electrical resistance was measured by the four-probe method using a Keithley nanovoltmeter (2182A) and precision current source (6220), and Seebeck coefficient was obtained from nanovoltmeter. The dimensions of nanoribbons were determined by Scanning Electron Microscope (SEM) and AFM. Data errors were estimated as ~8% for thermal conductivity, and ~5% for electrical conductivity and Seebeck coefficient. The length dependence of thermal conductance was performed for several nanoribbons from the same flake. Thermal contact resistance in the measurements is negligible.

Theoretical calculation. First-principles electronic structure calculations of TiS₃ were performed using density functional theory (DFT) within the generalized gradient approximation. The Perdew-Burke-Ernzerhof (PBE) form was used for the exchange-correlation functional.⁴⁹ The projector-augmented plane wave basis method as implemented in VASP (Vienna *ab initio* simulation package)⁵⁰ was used for all structural relaxations and supercell calculations for interatomic force constants. A 2×3×2 Monkhorst-Pack k -point grid and a plane wave energy cutoff of 500 eV was used for all structural relaxations. We used the DFT-D2 method as implemented in VASP for describing the weak vdW interaction between TiS₃ layers. The convergence threshold for energy and forces was set to 10⁻⁷ eV and

10^{-4} eV/Å, respectively. In the supercell calculations for obtaining harmonic (second order) interatomic force constants (IFCs) and anharmonic (third order) IFCs, Phonopy⁵¹ and ShengBTE code⁵² were used by taking into consideration non-analytical term correction and the force constant calculations were done with a same $2 \times 3 \times 2$ supercell and a $4 \times 3 \times 2$ q -point mesh, until convergence threshold above all was satisfied. The simulated lattice constants: $a = 4.97$ Å, $b = 3.93$ Å, $c = 8.80$ Å, are in consistency with literature.^{27, 53}

ASSOCIATED CONTENT

Supporting information

The Supporting Information includes additional Figures, Tables, and References.

AUTHOR INFORMATION

Corresponding Author

*Electronical mail: wuj@berkeley.edu, hongjw@bit.edu.cn, cld@mail.sic.ac.cn

Author Contributions

H.L. and J.W. conceive the project. H.L. designed the experiments, fabricated devices, and performed thermal and electrical measurements. X.Y. and J.H. performed the theoretical calculation. K.W. and S.T. provided the single crystal flake and SEM characterization of sample. H.L., X.Y., J.H. and J.W. discussed the data. H.L. and J.W. wrote the manuscript. All authors contributed to discussing the data and editing the manuscript. [§]These authors contributed equally to this work.

Notes

The authors declare no competing financial interest.

ACKNOWLEDGEMENTS

This work was supported by the Electronic Materials Program at the Lawrence Berkeley National Laboratory, which is supported by the Office of Science, Office of Basic Energy Sciences, of the U.S. Department of Energy under Contract No. DE-AC02-05CH11231. J.H. acknowledges the support from the National Science Foundation of China (Grant No. 11572040) and Beijing Natural Science Foundation (Grant No. Z190011). Theoretical calculations were performed using resources of National Supercomputer Center in Guangzhou. We thank Dr. Bin Chen for SEM characterization of sample. We thank Prof. Feng Wang and Dr. Saikat Mukhopadhyay for insightful discussions.

REFERENCES

- (1) Novoselov, K. S.; Geim, A. K.; Morozov, S. V.; Jiang, D.; Zhang, Y.; Dubonos, S. V.; Grigorieva, I. V.; Firsov, A. A. Electric field effect in atomically thin carbon films. *Science* **2004**, 306, (5696), 666-669.
- (2) Castro Neto, A. H.; Guinea, F.; Peres, N. M. R.; Novoselov, K. S.; Geim, A. K. The electronic properties of graphene. *Rev. Mod. Phys.* **2009**, 81, 109-162.
- (3) Mak, K. F.; Lee, C.; Hone, J.; Shan, J.; Heinz, T. F. Atomically Thin MoS₂: A New Direct-Gap Semiconductor. *Phys. Rev. Lett.* **2010**, 105, 136805.
- (4) Deng, D.; Novoselov, K. S.; Fu, Q.; Zheng, N.; Tian, Z.; Bao, X. Catalysis with two-dimensional materials and their heterostructures. *Nat. Nanotechnol.* **2016**, 11, (3), 218-230.
- (5) Bonaccorso, F.; Sun, Z.; Hasan, T.; Ferrari, A. C. Graphene photonics and optoelectronics. *Nat. Photonics* **2010**, 4, 611-622.
- (6) Wang, Q. H.; Kalantar-Zadeh, K.; Kis, A.; Coleman, J. N.; Strano, M. S. Electronics and optoelectronics of two-dimensional transition metal dichalcogenides. *Nat. Nanotechnol.* **2012**, 7, 669-712.
- (7) Roy, K.; Padmanabhan, M.; Goswami, S.; Sai, T. P.; Ramalingam, G.; Raghavan, S.; Ghosh, A. Graphene-MoS₂ hybrid structures for multifunctional photoresponsive memory devices. *Nat. Nanotechnol.* **2013**, 8, 826-830.
- (8) Britnell, L.; Ribeiro, R. M.; Eckmann, A.; Jalil, R.; Belle, B. D.; Mishchenko, A.; Kim, Y. J.; Gorbachev, R. V.; Georgiou, T.; Morozov, S. V.; Grigorenko, A. N.; Geim, A. K.; Casiraghi, C.; Castro Neto, A. H.; Novoselov, K. S. Strong Light-Matter Interactions in Heterostructures of Atomically Thin Films. *Science* **2013**, 340, 1311-1314.
- (9) Coleman, J. N.; Lotya, M.; O'Neill, A.; Bergin, S. D.; King, P. J.; Khan, U.; Young, K.; Gaucher, A.; De, S.; Smith, R. J.; Shvets, I. V.; Arora, S. K.; Stanton, G.; Kim, H.-Y.; Lee, K.; Kim, G. T.; Duesberg, G. S.; Hallam, T.; Boland, J. J.; Wang, J. J.; Donegan, J. F.; Grunlan, J. C.; Moriarty, G.; Shmeliov, A.; Nicholls, R. J.; Perkins, J. M.; Grievson, E.

M.; Theuwissen, K.; McComb, D. W.; Nellist, P. D.; Nicolosi, V. Two-Dimensional Nanosheets Produced by Liquid Exfoliation of Layered Materials. *Science* **2011**, 331, 568-571.

(10) Ho, C. Y.; Powell, R. W.; Liley, P. E. Thermal conductivity of the elements. *J. Phys. Chem. Ref. Data* **1972**, 1, (2), 279-421.

(11) Lee, S.; Yang, F.; Suh, J.; Yang, S.; Lee, Y.; Li, G.; Sung Choe, H.; Suslu, A.; Chen, Y.; Ko, C.; Park, J.; Liu, K.; Li, J.; Hippalgaonkar, K.; Urban, J. J.; Tongay, S.; Wu, J. Anisotropic in-plane thermal conductivity of black phosphorus nanoribbons at temperatures higher than 100 K. *Nat. Commun.* **2015**, 6, 8573.

(12) Liu, H.; Choe, H. S.; Chen, Y.; Suh, J.; Ko, C.; Tongay, S.; Wu, J. Variable range hopping electric and thermoelectric transport in anisotropic black phosphorus. *Appl. Phys. Lett.* **2017**, 111, (10), 102101.

(13) Chen, Y.; Chen, C.; Kealhofer, R.; Liu, H.; Yuan, Z.; Jiang, L.; Suh, J.; Park, J.; Ko, C.; Choe, H. S.; Avila, J.; Zhong, M.; Wei, Z.; Li, J.; Li, S.; Gao, H.; Liu, Y.; Analytis, J.; Xia, Q.; Asensio, M. C.; Wu, J. Black arsenic: a layered semiconductor with extreme in-plane anisotropy. *Adv. Mater.* **2018**, 30, (30), 1800754.

(14) Zhao, L.-D.; Lo, S.-H.; Zhang, Y.; Sun, H.; Tan, G.; Uher, C.; Wolverton, C.; Dravid, V. P.; Kanatzidis, M. G. Ultralow thermal conductivity and high thermoelectric figure of merit in SnSe crystals. *Nature* **2014**, 508, (7496), 373-377.

(15) Son, Y.-W.; Cohen, M. L.; Louie, S. G. Energy gaps in graphene nanoribbons. *Phys. Rev. Lett.* **2006**, 97, (21), 216803.

(16) Manzeli, S.; Ovchinnikov, D.; Pasquier, D.; Yazyev, O. V.; Kis, A. 2D transition metal dichalcogenides. *Nature Reviews Materials* **2017**, 2, 17033.

(17) Jin, Y.; Li, X.; Yang, J. Single layer of MX₃ (M = Ti, Zr; X = S, Se, Te): a new platform for nano-electronics and optics. *Phys. Chem. Chem. Phys.* **2015**, 17, (28), 18665-18669.

(18) Island, J. O.; Biele, R.; Barawi, M.; Clamagirand, J. M.; Ares, J.

R.; Sánchez, C.; Zant, H. S. J. v. d.; Ferrer, I. J.; D'Agosta, R.; Castellanos-Gomez, A. Titanium trisulfide (TiS₃): a 2D semiconductor with quasi-1D optical and electronic properties. *Sci. Rep.* **2016**, *6*, 22214.

(19) Gorlova, I. G.; Pokrovskii, V. Y.; Zybtssev, S. G.; Titov, A. N.; Timofeev, V. N. Features of the conductivity of the quasi-one-dimensional compound TiS₃. *J. Exp. Theor. Phys* **2010**, *111*, (2), 298-303.

(20) Furuseth, S.; Brattaas, L.; Kjekshus, A. On the crystal structures of TiS₃, ZrS₃, ZrSe₃, ZrTe₃, HfS₃, and HfSe₃. *Acta Chem. Scand. A* **1975**, *29*, (6), 623-631.

(21) Ferrer, I. J.; Ares, J. R.; Clamagirand, J. M.; Barawi, M.; Sánchez, C. Optical properties of titanium trisulphide (TiS₃) thin films. *Thin Solid Films* **2013**, *535*, 398-401.

(22) Kang, J.; Wang, L.-W. Robust band gap of TiS₃ nanofilms. *Phys. Chem. Chem. Phys.* **2016**, *18*, (22), 14805-14809.

(23) Dai, J.; Zeng, X. C. Titanium trisulfide monolayer: theoretical prediction of a new direct-gap semiconductor with high and anisotropic carrier mobility. *Angew. Chem. Int. Ed.* **2015**, *54*, (26), 7572-7576.

(24) Lipatov, A.; Wilson, P. M.; Shekhirev, M.; Teeter, J. D.; Netusil, R.; Sinitiskii, A. Few-layered titanium trisulfide (TiS₃) field-effect transistors. *Nanoscale* **2015**, *7*, (29), 12291-12296.

(25) Island, J. O.; Barawi, M.; Biele, R.; Almazán, A.; Clamagirand, J. M.; Ares, J. R.; Sánchez, C.; van der Zant, H. S. J.; Álvarez, J. V.; D'Agosta, R.; Ferrer, I. J.; Castellanos-Gomez, A. TiS₃ transistors with tailored morphology and electrical properties. *Adv. Mater.* **2015**, *27*, (16), 2595-2601.

(26) Wu, K.; Torun, E.; Sahin, H.; Chen, B.; Fan, X.; Pant, A.; Wright, D. P.; Aoki, T.; Peeters, F. M.; Soignard, E.; Tongay, S. Unusual lattice vibration characteristics in whiskers of the pseudo-one-dimensional titanium trisulfide TiS₃. *Nat. Commun.* **2016**, *7*, 12952.

- (27) Zhang, J.; Liu, X.; Wen, Y.; Shi, L.; Chen, R.; Liu, H.; Shan, B. Titanium trisulfide monolayer as a potential thermoelectric material: a first-principles-based boltzmann transport study. *ACS Appl. Mater. Interfaces* **2017**, *9*, (3), 2509-2515.
- (28) Furuseth, S.; Fjellvåg, H.; Johansson, L.-G.; Gulyai, V. P.; Persson, I.; Elding, L. I. Re-examination of the crystal structure of $ZrTe_3$. *Acta Chem. Scand.* **1991**, *45*, 694-697.
- (29) Fleet, M. E.; Harmer, S. L.; Liu, X.; Nesbitt, H. W. Polarized X-ray absorption spectroscopy and XPS of TiS_3 : S K- and Ti L-edge XANES and S and Ti 2p XPS. *Surf Sci.* **2005**, *584*, (2), 133-145.
- (30) Cordero, B.; Gómez, V.; Platero-Prats, A. E.; Revés, M.; Echeverría, J.; Cremades, E.; Barragán, F.; Alvarez, S. Covalent radii revisited. *Dalton Transactions* **2008**, (21), 2832-2838.
- (31) Silva-Guillén, J. A.; Canadell, E.; Ordejón, P.; Guinea, F.; Roldán, R. Anisotropic features in the electronic structure of the two-dimensional transition metal trichalcogenide TiS_3 : electron doping and plasmons. *2D Mater.* **2017**, *4*, (2), 025085.
- (32) Shi, L.; Li, D.; Yu, C.; Jang, W.; Kim, D.; Yao, Z.; Kim, P.; Majumdar, A. Measuring thermal and thermoelectric properties of one-dimensional nanostructures using a microfabricated device. *J. Heat Transfer* **2003**, *125*, (5), 881-888.
- (33) Li, D.; Wu, Y.; Kim, P.; Shi, L.; Yang, P.; Majumdar, A. Thermal conductivity of individual silicon nanowires. *Appl. Phys. Lett.* **2003**, *83*, (14), 2934-2936.
- (34) Lee, S.; Hippalgaonkar, K.; Yang, F.; Hong, J.; Ko, C.; Suh, J.; Liu, K.; Wang, K.; Urban, J. J.; Zhang, X.; Dames, C.; Hartnoll, S. A.; Delaire, O.; Wu, J. Anomalously low electronic thermal conductivity in metallic vanadium dioxide. *Science* **2017**, *355*, (6323), 371-374.
- (35) Hu, J.; Ruan, X.; Chen, Y. P. Thermal Conductivity and Thermal Rectification in Graphene Nanoribbons: A Molecular Dynamics Study. *Nano Lett.* **2009**, *9*, (7), 2730-2735.
- (36) Broido, D. A.; Malorny, M.; Birner, G.; Mingo, N.; Stewart, D. A.

Intrinsic lattice thermal conductivity of semiconductors from first principles. *Appl. Phys. Lett.* **2007**, 91, (23), 231922.

(37) Ashcroft, N. W.; Mermin, N. D., *Solid State Physics*. Holt, Rinehart and Winston: New York, 1976.

(38) Tian, Z.; Garg, J.; Esfarjani, K.; Shiga, T.; Shiomi, J.; Chen, G. Phonon conduction in PbSe, PbTe, and PbTe_{1-x}Se_x from first-principles calculations. *Phys. Rev. B* **2012**, 85, (18), 184303.

(39) Li, W.; Lindsay, L.; Broido, D. A.; Stewart, D. A.; Mingo, N. Thermal conductivity of bulk and nanowire Mg₂Si_xSn_{1-x} alloys from first principles. *Phys. Rev. B* **2012**, 86, (17), 174307.

(40) Mukhopadhyay, S.; Lindsay, L.; Singh, D. J. Optic phonons and anisotropic thermal conductivity in hexagonal Ge₂Sb₂Te₅. *Sci. Rep.* **2016**, 6, 37076.

(41) Kittel, C., *Introduction to Solid State Physics*. 7th Edition ed.; Wiley: New York, 1996.

(42) Lindsay, L.; Broido, D. A.; Reinecke, T. L. First-principles determination of ultrahigh thermal conductivity of boron arsenide: a competitor for diamond? *Phys. Rev. Lett.* **2013**, 111, (2), 025901.

(43) Bies, W. E.; Radtke, R. J.; Ehrenreich, H. Phonon dispersion effects and the thermal conductivity reduction in GaAs/AlAs superlattices. *J. Appl. Phys.* **2000**, 88, (3), 1498-1503.

(44) Gonze, X.; Lee, C. Dynamical matrices, Born effective charges, dielectric permittivity tensors, and interatomic force constants from density-functional perturbation theory. *Phys. Rev. B* **1997**, 55, (16), 10355-10368.

(45) Qin, G.; Yan, Q.-B.; Qin, Z.; Yue, S.-Y.; Hu, M.; Su, G. Anisotropic intrinsic lattice thermal conductivity of phosphorene from first principles. *Phys. Chem. Chem. Phys.* **2015**, 17, (7), 4854-4858.

(46) Hellman, O.; Broido, D. A. Phonon thermal transport in Bi₂Te₃ from first principles. *Phys. Rev. B* **2014**, 90, (13), 134309.

(47) Guo, R.; Wang, X.; Kuang, Y.; Huang, B. First-principles study

of anisotropic thermoelectric transport properties of IV-VI semiconductor compounds SnSe and SnS. *Phys. Rev. B* **2015**, 92, (11), 115202.

(48) Wehmeyer, G.; Yabuki, T.; Monachon, C.; Wu, J.; Dames, C. Thermal diodes, regulators, and switches: physical mechanisms and potential applications. *Appl. Phys. Rev.* **2017**, 4, (4), 041304.

(49) Perdew, J. P.; Burke, K.; Ernzerhof, M. Generalized Gradient Approximation Made Simple. *Phys. Rev. Lett.* **1996**, 77, (18), 3865-3868.

(50) Kresse, G.; Furthmüller, J. Efficient iterative schemes for ab initio total-energy calculations using a plane-wave basis set. *Phys. Rev. B* **1996**, 54, (16), 11169-11186.

(51) Togo, A.; Oba, F.; Tanaka, I. First-principles calculations of the ferroelastic transition between rutile-type and CaCl₂-type SiO₂ at high pressures. *Phys. Rev. B* **2008**, 78, (13), 134106.

(52) Li, W.; Carrete, J.; A. Katcho, N.; Mingo, N. ShengBTE: A solver of the Boltzmann transport equation for phonons. *Comput. Phys. Commun.* **2014**, 185, (6), 1747-1758.

(53) Wu, J.; Wang, D.; Liu, H.; Lau, W.-M.; Liu, L.-M. An ab initio study of TiS₃: a promising electrode material for rechargeable Li and Na ion batteries. *RSC Advances* **2015**, 5, (28), 21455-21463.